PAPER

Boosting the syngas production of a SrTiO₃ photocathode *via* plasmonic hot electron injection from an Ag underlayer

Galyam Sanfo,†[a] Aejaz Ul Bashir,†[b] Nusrat Rashid†,[a] Siming Huang,[a]
Pravin Popinand Ingole 🔾 *[b] and Mojtaba Abdi-Jalebi 🔾 *[a]

Photoelectrochemical (PEC) CO_2 reduction offers a promising pathway for sustainable fuel generation powered by sunlight. However, current PEC systems face two major challenges: inefficient charge separation and limited visible-light absorption in conventional semiconductor photocatalysts. In this study, we addressed these limitations through an innovative material design that integrates plasmonic silver nanostructures with a SrTiO₃ perovskite, creating a high-performance and durable hybrid photocathode for CO_2 reduction. The hybrid photocathode was fabricated *via* the spin-coating of a SrTiO₃ film and the deposition of a thin plasmonic silver layer—either as an underlayer or an overlayer—using physical vapor deposition (PVD). Notably, the silver underlayer beneath SrTiO₃ demonstrated remarkable performance under back illumination. The silver film served dual functions: it extended light absorption into the visible spectrum through the localized surface plasmon resonance (LSPR) and simultaneously suppressed charge recombination. This synergistic effect delivered exceptional CO_2 reduction activity, achieving 80% faradaic efficiency for CO production at a low potential of -0.8 V *vs.* RHE, with a CO generation rate of 12 μmol h^{-1} mg^{-1}—three times higher than that of pristine SrTiO₃. These findings establish plasmonic-perovskite hybrids as a promising platform for solar fuel generation, combining the stability of oxide semiconductors with the optical tunability of metal nanostructures—achieved here by embedding the metal layer beneath the semiconductor. The design principles demonstrated can be extended to other photocatalytic systems for renewable energy applications.

1 Introduction

The increasing concentration of carbon dioxide (CO_2) in the atmosphere, primarily due to fossil fuel combustion and industrial activities, has led to severe environmental challenges, including global warming and ocean acidification.[1] Innovative approaches for CO_2 capture, storage, and conversion into value-added chemicals and fuels are being explored to mitigate these effects. Among these approaches, photoelectrochemical CO_2 reduction (PECCR) has gained significant attention as it offers a sustainable way to utilize sunlight and electricity to convert CO_2 into hydrocarbons, alcohols, or syngas.[2] This process helps reduce greenhouse gas emissions and provides a pathway for producing renewable fuels, thereby addressing environmental and energy concerns. However, achieving a high solar-to-chemical efficiency and selectivity in PEC CO_2 reduction

remains a major challenge, necessitating the development of advanced materials with superior catalytic and light-absorption properties.[3]

In recent years, titanium-based perovskite oxides, such as strontium titanate (SrTiO₃) and barium titanate (BaTiO₃), have emerged as promising photocatalysts for CO_2 reduction due to their excellent chemical stability, suitable band edge positions, and ability to drive multi-electron transfer reactions.[4,5] SrTiO₃ has been widely studied due to its high conduction band potential, which enables efficient CO_2 reduction.[6] However, its fast electron–hole pair recombination rate limits its utilization as an efficient photocathode due to the unavailability of its charge carriers for the reaction.[7] Moreover, its wide bandgap (~3.2 eV) limits absorption to only the ultraviolet (UV) region.[8] This necessitates modifications, such as doping, heterostructure formation, and surface engineering, to enhance the visible-light-enhanced PEC activity. Interestingly, introducing oxygen vacancies (O_v) and coupling SrTiO₃ with plasmonic nanoparticles, such as Ag, Cu, or Au, can improve charge separation, modulate the Fermi level, and regulate the selectivity toward the desired CO_2 reduction products.[9,10]

[a]Institute for Materials Discovery, University College London, Malet Place, London, WC1E 7JE, UK. E-mail: m.jalebi@ucl.ac.uk

[b]Department of Chemistry, Indian Institute of Technology Delhi, Hauz Khas, New Delhi, 110016, India. E-mail: ppingole@chemistry.iitd.ac.in

† The authors contributed equally.

Recent reviews have underscored the potential of plasmonic-metal heterostructures in modulating CO_2 conversion pathways *via* localised surface plasmon resonances (LSPR) and hot electron injection.[11] By carefully tuning particle size, morphology, and interface chemistry, high solar fuel yields were recorded under visible illumination.[12] Systems, such as Au-$SrTiO_3$, benefit from strong visible LSPR and chemical robustness and have demonstrated enhanced H_2 evolution and CO_2 reduction.[13] However, these systems rely on scarce and expensive noble metals and are typically realised as nanoparticle decorations rather than scalable underlayer architectures. Conversely, Cu- or CuO-modified $SrTiO_3$ offers lower cost and extended visible absorption *via* narrow-gap oxides and p–n heterojunction formation, but suffers from photocorrosion and a less defined plasmonic response under reductive conditions.[14] In contrast, the Ag underlayer employed in this study combines the strong visible-range plasmonic response of Ag with a continuous metallic back contact, which simultaneously (i) enhances local electromagnetic fields at the $SrTiO_3$ interface, (ii) increases optical path length through reflective coupling, and (iii) provides an efficient, low-resistance, electron-transfer pathway. This architecture thus balances plasmonic performance, stability, and economic viability in a way that is difficult to achieve with Au or Cu-based $SrTiO_3$ hybrids.[15]

As such, a lot of attention has been given to materials capable of supporting localized surface plasmon resonance due to their unique ability to enhance light absorption, generate energetic hot charge carriers, and create intense localized electromagnetic fields. These effects collectively amplify the efficiency of photoelectrochemical CO_2 reduction reactions (PECRR).[16] Fundamentally, LSPR arises from the resonant oscillation of conduction electrons in metal nanostructures when excited by light at specific wavelengths. This resonance not only broadens the light absorption spectrum—especially into the visible range—but also facilitates the generation of hot electrons that can cross the Schottky barrier formed at metal/semiconductor interfaces. These Schottky barriers act as effective electron traps, preventing rapid recombination by separating charge carriers and prolonging electron lifetime within the semiconductor.[17] The extended lifetime enhances the semiconductor's catalytic capability, improving the overall photocatalytic efficiency.[10] These advancements in Ti-based perovskites hold great potential for scalable PEC systems that can efficiently convert CO_2 into sustainable fuels, contributing to the transition towards a carbon-neutral energy future. Recent studies have further expanded the collective understanding of catalytic pathways and material design for efficient CO_2 electroreduction and photoreduction. For example, new catalyst materials with atomic-level interface control have demonstrated enhanced selectivity towards complex hydrocarbons and alcohols under mild operating conditions.[18] Advances in understanding interfacial charge dynamics and reaction intermediate stabilisation within engineered metal-oxide catalysts continue to drive improvements in faradaic efficiency and product distribution.[19]

Despite notable advancements, LSPR-coupled Ti-based perovskites still encounter key challenges on two major fronts. From a photochemical standpoint, issues, such as the photocorrosion of plasmonic components, nanoparticle aggregation, and difficulties in precisely controlling particle size and morphology continue to hinder PEC performance. Electrochemically, these systems often suffer from low reaction rates, limited product selectivity, and inadequate long-term operational stability.[20–22] Emerging evidence points to the critical role of catalyst surface engineering and encapsulation strategies in mitigating photocorrosion and promoting long-term durability under operational conditions.[23] These insights highlight the necessity of integrating plasmonic enhancement mechanisms with robust support materials to achieve synergistic improvements in activity and stability.

To address these challenges, we have developed a series of thin-film catalysts comprised of STO, which provided electrolyte-induced corrosion resistance, combined with a 30 nm thin silver (Ag) film as an LSPR generator. The catalysts were fabricated *via* a combination of a spin-coating technique and physical vapour deposition for efficient CO_2 reduction. Two photocathode analogues were fabricated based on the differing layer architectures relative to the STO layer. The FTO-Ag-STO (UL-Ag-STO) configuration integrates a plasmonic silver film as an underlayer beneath a $SrTiO_3$ semiconductor film, whilst the FTO-STO-Ag (OL-Ag-STO) integrates a plasmonic silver film on top of $SrTiO_3$ to unravel the inhibition of dynamic charge transportation due to interfacial silver oxidation. Furthermore, we assessed which type of illumination best enhanced the concurrent photocurrents, which corroborated the significance of device architecture in PEC assemblies.

The UL-Ag-STO photocathodes demonstrated superior activity when operated under back-illumination conditions. By leveraging silver's localized surface plasmon resonance (LSPR),[24,25] the hybrid catalyst significantly extended the light-absorption range into the visible spectrum, while simultaneously generating energetic hot electrons.[26,27] These hot carriers overcame the Schottky barrier at the Ag/STO interface,[28,29] and were injected into the semiconductor, enabling efficient charge separation.[30] The Schottky barrier further acted as an electron trap, suppressing recombination and prolonging the charge-carrier lifetime.[31,32] Coupled with back illumination through the transparent substrate, this configuration maximized plasmonic excitation and enhanced interfacial charge transfer, achieving a faradaic efficiency of 80% and a CO production rate of 12 $\mu mol\ h^{-1}\ mg^{-1}$ at -0.8 V *vs.* RHE, thus extending STO's performances as a photocathode.

2 Experimental section

2.1 Materials and chemicals

All chemicals were analytical grade and used without purification unless stated otherwise. $Sr(OH)_2\cdot8H_2O$, KH_2PO_4, K_2HPO_4, NaOH, and TiO_2 (21 nm, $\geq$99%) were procured from Merck, India. FTO substrates were obtained from Alfa Aesar. Silver granules were purchased from Sigma Aldrich. Ultrapure Ar and N_2 gases from Sigma Gases, New Delhi, were passed through moisture and oxygen traps, and gas purification panels before they were used for the PEC experiments.

3 Synthesis and fabrication of SrTiO₃ (STO) and Ag/STO catalysts

Pristine STO was synthesized following a literature-reported, one-step hydrothermal method using TiO_2, $Sr(OH)_2 \cdot 8H_2O$, and NaOH for the hydrolytic attack on the Ti–O bond as per the following equations:[32]

$$TiO_2 + 2H_2O + 2OH^- \rightarrow [Ti(OH)_6]^{2-} \quad (1)$$

$$Sr^{2+} + [Ti(OH)_6]^{2-} \rightarrow SrTiO_3 + 3H_2O \quad (2)$$
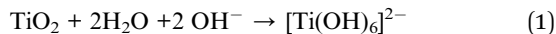
After continuous stirring for *ca.* 20 min, a mixture of 12.5 mmol of $Sr(OH)_2 \cdot 8H_2O$, 12.5 mmol of TiO_2, and 50 mL of 5 M NaOH was transferred into a Teflon-lined hydrothermal autoclave of 100 mL capacity and heated at 180 °C for *ca.* 15 h. The obtained white product was centrifuged, washed several times with water, acetone, and HCl, and then dried in a vacuum oven at 70 °C for about 24 hours before using it for physico-chemical and electrochemical investigations.

3.1 Synthesis of Ag-SrTiO₃ heterojunctions

For the synthesis of the samples, a 6 mg mL^{-1} solution of strontium titanate (STO) was first prepared in isopropyl alcohol (IPA) and sonicated to achieve a uniform dispersion. Each sample was fabricated by spin-coating 100 μL of the STO dispersion onto the substrate for 20 seconds at 2500 rpm; this process was repeated a total of five times to improve uniformity in the surface coverage. For the deposition of silver (Ag) on the fluorine-doped tin oxide (FTO) substrates, a thickness of 30 nm was selected and deposition was achieved using a nanoparticle physical vapor deposition system (nanoPVD). Based on the different sample architectures, two sets of samples were prepared: in the first set, the FTO substrates were coated with the STO layers as described above, after which Ag was deposited on top; thus, completing the fabrication of the FTO/STO/Ag films (OL-Ag-STO). In the second set, an Ag overlayer was first deposited onto the FTO substrates before the sequential deposition of the STO layers, thus resulting in the fabrication of the FTO/Ag/STO films (UL-Ag-STO). This synthesis strategy (as well as the individual constituents comprising FTO/STO and FTO/Ag) allowed for a direct comparison of the effects of Ag positioning relative to the STO layer and its modulation of the electronic properties.

4 Material characterization

X-ray diffraction (XRD) measurements were acquired using an AERIS PANalytical Research Edition instrument. The setup employed Cu Kα radiation ($\lambda = 0.154$ nm) at 40 kV and 7.5 mA with scanning from 10° to 70°. Raman spectroscopy measurements were then performed using a Renishaw inVia Raman microscope (Renishaw, UK). The samples were analyzed with a 515 nm laser excitation source. Lastly, sample surface morphologies were analyzed using a Hitachi™4000II Scanning Electron Microscope (SEM) to observe surface variations. KPFM

measurements were carried out using an SKP5050 KP Technology System (tapping mode) by measuring the contact potential differences between the various samples and the KPFM tip. The work function for all the samples was calculated using the following equation:

$$\varphi_{sample} = \varphi_{tip} - e \, (S.P) \quad (3)$$

where φ_{sample} denotes the respective work function of the samples determined from the surface potential data (S.P), whilst φ_{tip} represents the calibrated work function value of the KPFM tip (4.97 eV).

5 PEC evaluation and product quantification

Photoelectrochemical measurements were conducted using Autolab 302 and CHI workstations in a Teflon-lined, two-chamber, three-electrode setup with a quartz window. The cathodic chamber contained a catalyst-modified FTO working electrode, Ag/AgCl reference electrode in phosphate-buffered saline (PBS, pH 7), an anodic chamber of Pt mesh as a counter electrode in 0.2 M KOH (pH 13) coupled *via* a Nafion 117 membrane. The electrolytes were purged with ultrapure Ar and CO_2 (flow rate: 20 sccm) before measurements. The potentials were converted to RHE using the equation: $E_{RHE} = E_{Ag/AgCl,Cl^-\,(sat.KCl)} + 0.197 + 0.059$ pH. The gaseous products (H_2 and CO) were analysed by gas chromatography, with faradaic efficiency and yield rates calculated using eqn (3) and (4), respectively.[33]

$$\%F.E_g = \frac{n_e \times C_{ppm} \times F \times f_m \times P}{R \times T \times i} \times 100 \quad (4)$$

$$R_P \left(mol\ mg_{cat}^{-1}\ s^{-1} \right) = \frac{n_e \times N_p \times F}{t} \quad (5)$$

where n_e is the number of electrons required for one molecule of product, C_{ppm} is the ppm of the gaseous product formed, N_p is the number of moles of a liquid product, P is the ambient pressure (101, 325 N m^{-2}), f_m is the molar flow rate (sccm mole^{-1}), T is the ambient temperature, F is the Faraday constant (96,485 C mol^{-1}), R is the gas constant (8.314 J K^{-1} mol^{-1}), R_P (mole mg$_{cat}^{-1}$s^{-1}) is the yield rate of a particular product, and i is the average current. Additional details about the F.E$_g$ calculations are mentioned in the SI.

6 Results and discussion

6.1 Structural characterizations

The resulting strontium titanate powder obtained following Fig. 1a was first evaluated based on its crystal morphology, which is sensitive to synthesis conditions.[32,34] The DFT studies show that the crystallographic facets and atomic terminations were derived from the unique atomic configurations which resulted in distinctive facets.[32,35] Most notably, those facets had different surface energies and favored anisotropic charge separation and transfer towards these surface terminations. To
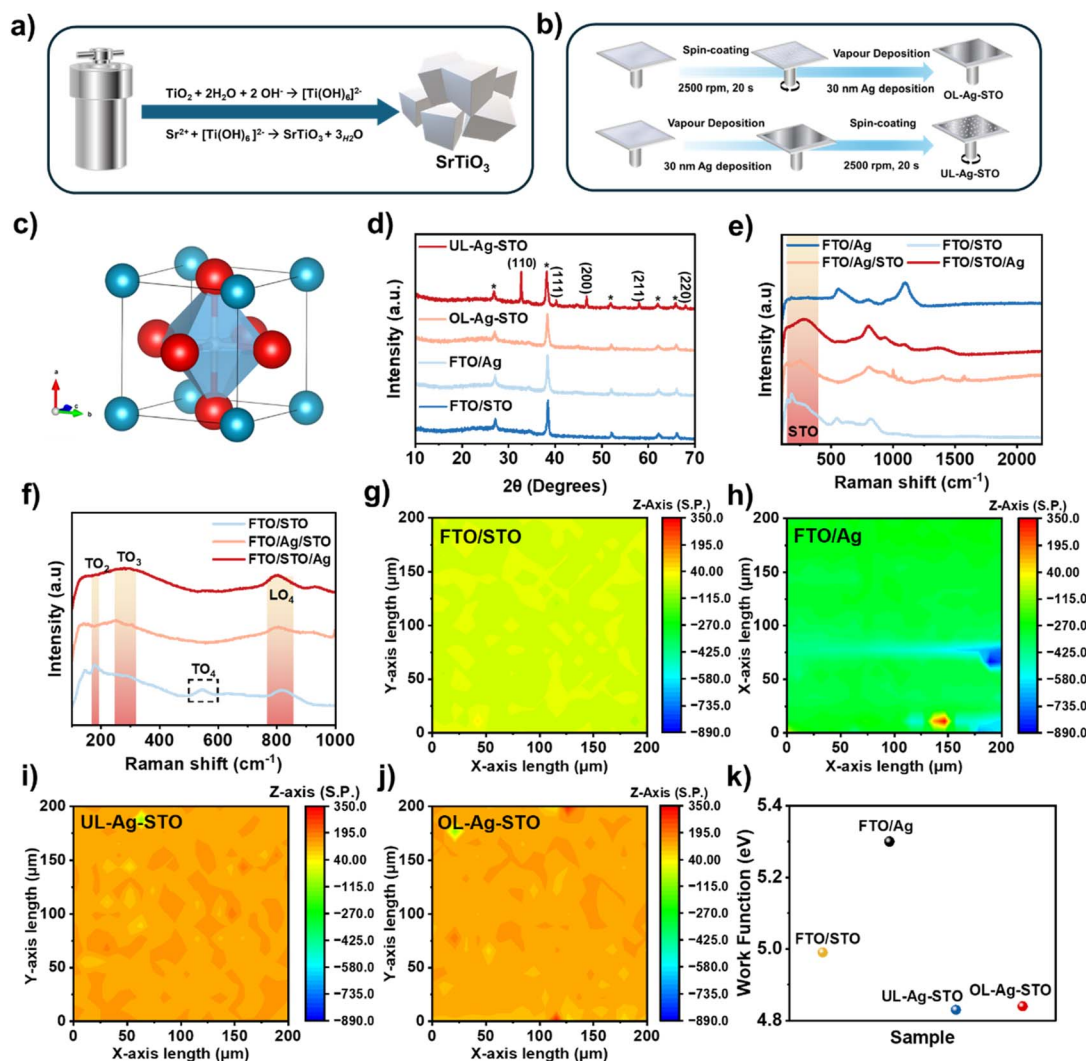
Fig. 1 (a) One-step autoclave synthesis of STO. (b) Step-by-step fabrication of the OL-Ag-STO and UL-Ag-STO photocathode heterostructures *via* spin-coating and physical vapor deposition. (c) Crystal structure of the cubic perovskite phase space group *Pm3m*. (d) X-ray diffraction patterns of UL-Ag-STO and OL-Ag-STO. (d–f) Ensuing variations in the Raman spectral response relative to the differences in architectures. (g–j) Surface potential variations in FTO/STO, FTO/Ag, UL-Ag-STO, and OL-Ag-STO, respectively. (k) Work function differences extrapolated from the average surface potential differences obtained from (f–i).

identify these, the XRD pattern illustrated in Fig. 1c provides further insight into the structural characteristics of these titanium-based materials. The diffraction peaks obtained from the UL-Ag-STO films corresponded well with the characteristic cubic perovskite phase (space group *Pm3m*), consistent with literature values. Key diffraction angles are observed at 22.85°, 32.20°, 39.84°, 46.28°, 57.10°, and 67.40°, which were assigned to the (100), (110), (111), (200), (211), and (220) planes of STO, respectively.[36] The presence of silver did not cause noticeable shifts in the STO diffraction peaks, indicating that the underlying STO crystal structure remained intact and unaffected by the Ag overlayer. This observation confirms that the Ag film did not alter the fundamental lattice parameters or crystalline phase of STO, thereby demonstrating the structural stability of STO upon integration with the Ag plasmonic layer.[37]

Raman spectroscopy was then employed to assess the chemical bond signature of the concurrent heterostructures.

We observed a combination of vibrational modes from both Ag and STO, as depicted in Fig. 1d and e. The STO component exhibits characteristic vibrational peaks at 178, 282.4, 545, and 802 cm^{-1}, which describe the first-order phonon modes, TO_2, TO_3, TO_4, and LO_4, associated with the O–Sr–O bending modes, and the Ti–O–Ti bending and stretching modes, respectively.[38–40] The Raman spectra for the UL-Ag-STO and OL-Ag-STO heterostructures revealed more complex modifications in their vibrational properties compared to the FTO/STO reference. Notably, the characteristic STO peak at approximately 545 cm^{-1} disappeared in both the Ag-containing structures, regardless of the stacking order. Although the low-frequency region associated with STO can still be identified in these samples, a significant drop in intensity was observed in the spectral region where the STO peak was previously prominent. These observations strongly suggest that the incorporation of the Ag underlayer onto STO significantly modified charge

transfer and resulted in strong electronic interactions at the interface.[41,42] This led to the formation of collective phonon-plasmon-mediated modes, wherein the Ag-coupled STO exhibited hybridized modes, which are observed in the Raman spectra and likely reflect a complex interplay between the metallic electronic states and STO lattice. This mechanism not only highlights the modifications in the interfacial vibrational signature, but also sets the stage for alternative ways of boosting charge transport and the creation of extra electron–hole pairs.[43]

To complement our previous observation and better understand the interactions between STO and the Ag films, KPFM was used to extrapolate the work function from the average distribution of the surface potential associated with the various samples. Fig. 1g to j depict surface potential variations along a 200 μm × 200 μm surface area. Subsequent histogram distributions were used to obtain the average surface potential (Fig. S1a–d) and thus calculate the work function.

The average surface potential of FTO/STO and FTO/Ag were calculated to be −15.21 mV and −326.6 mV, resulting in a work function of 4.99 eV and 5.3 eV, respectively. With an average SP of 137.6 mV for UL-Ag-STO and 131.8 mV for UL-Ag-STO, both these heterostructure samples exhibited lower work function values of 4.83 eV and 4.84 eV, respectively (Fig. 1k). This reduction in the work function is in good agreement with the expected interfacial effects derived from the electronic redistribution due to charge-transfer processes, which arose from

the Fermi level equilibration associated with Ag and STO, allowing for a higher electron density near the interface of the heterostructure, resulting in a higher CO_2 reduction.[44,45]

Furthermore, both OL-Ag-STO and UL-Ag-STO demonstrate negligible differences in their work function, suggesting that the stacking order did not influence the overall surface electronic density.[46] Therefore, we can conclude that the deposition of the conductive Ag film played a pivotal role in facilitating charge redistribution by modulating the interfacial electronic density *via* Fermi equilibration because of charge transfer.[28,46]

We then concurrently employed field emission scanning electron microscopy (FESEM) imaging to observe the STO morphology of the UL-Ag-STO photocathodes, and elemental mapping from energy-dispersive X-ray spectroscopy (EDS/EDAX) to accurately quantify elemental distribution, as shown in Fig. 2. The FESEM images in Fig. 2a–c show largely cuboidal STO structures with a mean size of 100 nm, which were dispersed on either FTO or the plasmonic silver film. EDS (Fig. 2d–h) was then employed to analyze the elemental composition of the UL-Ag-STO heterostructure, providing both qualitative and quantitative information about oxygen (O), titanium (Ti), strontium (Sr), and silver (Ag). The EDS results further support the presence of Ag alongside the expected constitutional elements of perovskite $SrTiO_3$. Quantitative analysis based on atomic percentages normalized to Ti yielded an approximate empirical formula of $Sr_{(0.81)}$, $Ti_{(1)}$, $O_{(4.05)}$ and

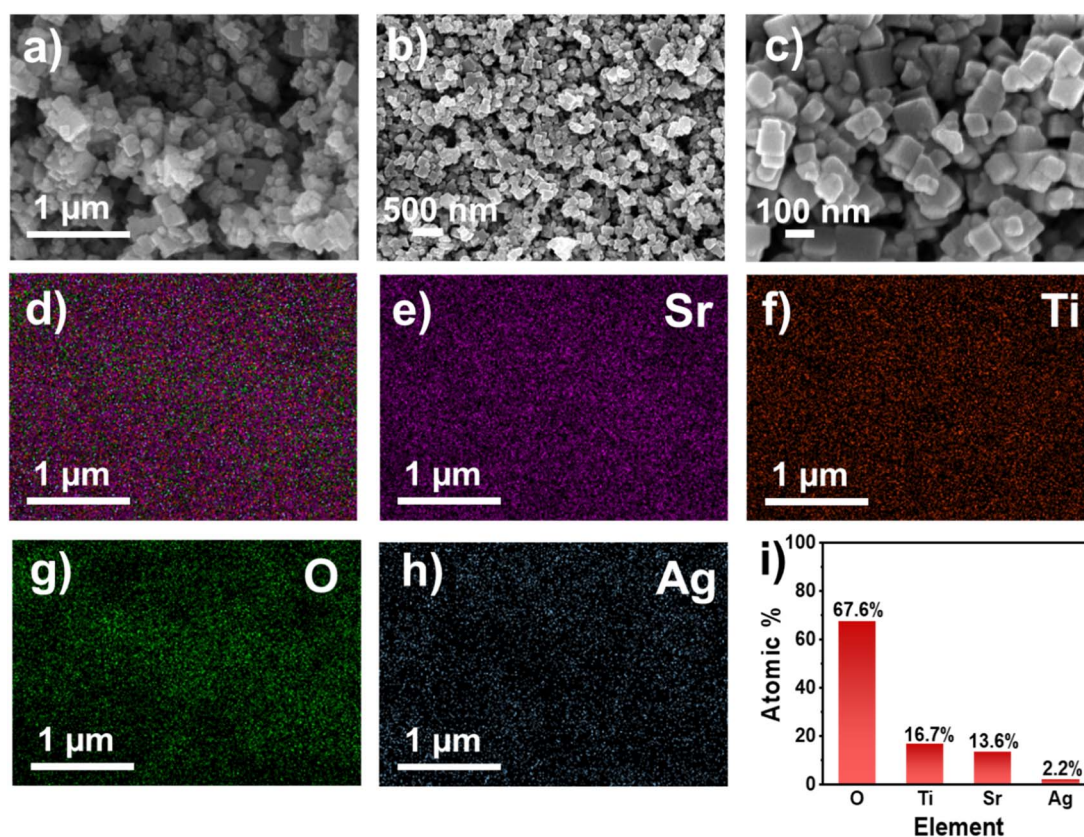**Fig. 2** (a–c) Selected FESEM images of the UL–Ag–STO films. Figures (b) and (c) show the distributed STO crystals within the 500 nm and 100 nm inset magnifications, respectively. (d–h) EDS elemental mapping highlighting the elemental distributions of STO and underlying Ag in UL–Ag–STO films relative to the FESEM of figure (a). (i) Subsequent atomic ratios tabulated from the EDS spectra.

$Ag_{(0.13)}$ with respective error margins of ± 0.05, ± 0.46, ± 0.001 for Sr, O, and Ag, respectively. The overarching results indicate that the STO layer remained close to its ideal stoichiometry with a slight Sr deficiency and minor oxygen measurement variation, both of which are commonly expected due to instrumental limitations and surface sensitivity. The presence of silver at approximately 13% relative Ti, confirms its incorporation as a discrete layer without disturbing the superposed STO elemental composition.

6.2 Photoelectrochemical investigations

The primary PEC activity of the designed photocathodes was investigated *via* cyclic voltammetry (CV), impedance spectroscopy (EIS), and light-chopped chronoamperometry (CA) in PBS under dark and light conditions. Under light illumination in the

CO_2-saturated PBS, UL-Ag-STO showed an enhanced current density with an anodic shift (20 mV) and an onset potential of 0.5 mA cm^{-2} compared to the Ar-saturated PBS in the presence and absence of light (Fig. 3a). All the CV spectra show two redox peaks appearing between -0.089 V and -0.168 V vs. RHE, arising from the Ag/Ag–OH or Ag/Ag–O redox processes. Although the underlying redox chemistry is the same, the number, position, and sharpness of these peaks changed under different experimental conditions due to changes in the local environment at the UL-Ag-STO-PBS interface. For instance, under Ar and dark conditions, the interface remained in its most electronically uncomplicated state, without photogenerated carriers or CO_2-related surface chemistry; hence, a single, well-defined Ag redox feature was observed around -0.109 V vs. RHE, again attributed to the Ag$^+$/Ag redox system. In contrast, under illumination and/or in the presence of CO_2, several
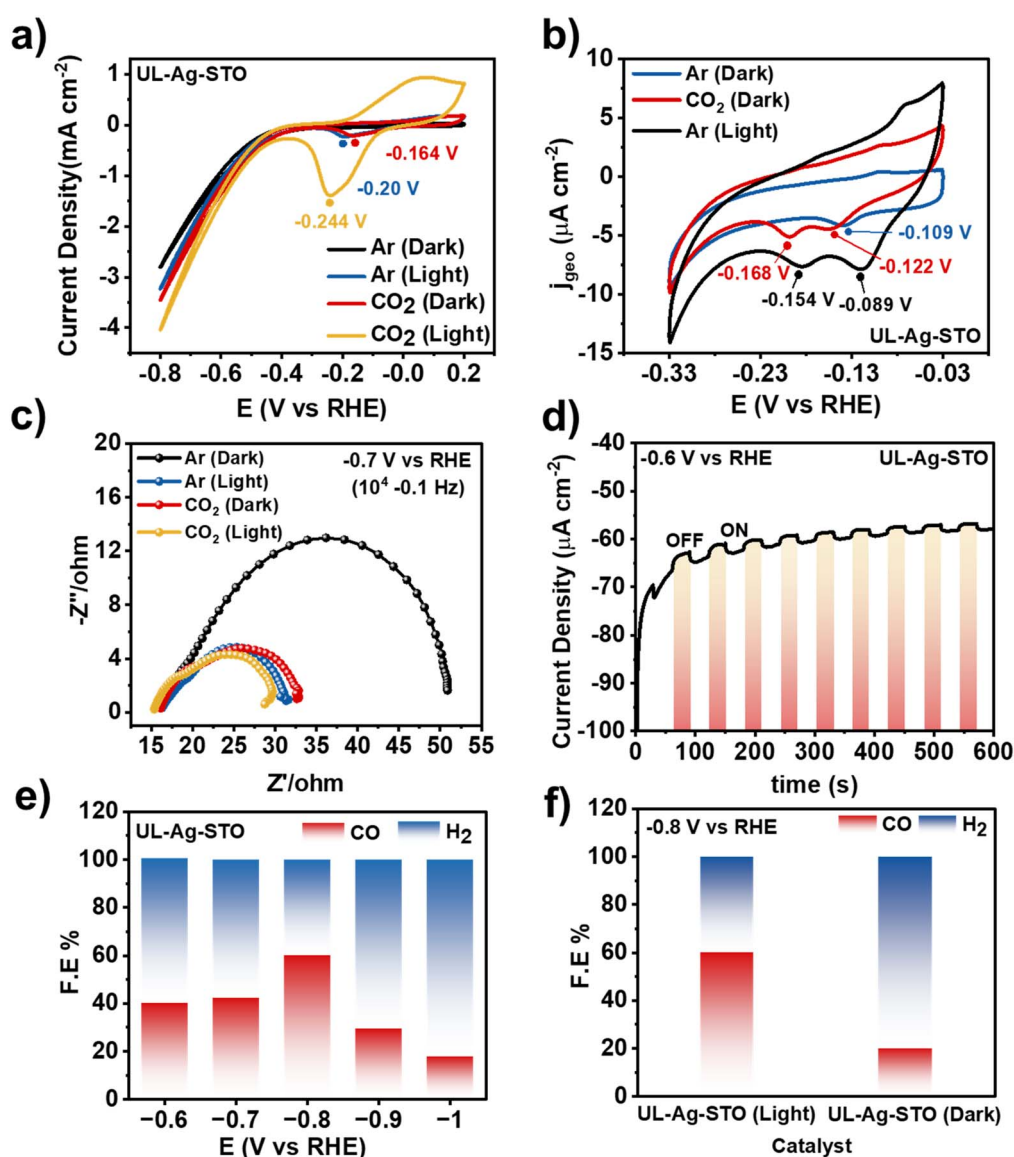

Fig. 3 Photoelectrochemical response of UL-Ag-STO. (a) Cyclic voltammetry (CV) and consequent redox peak under various conditions, (b) zoomed view of Fig. 3(a) showing redox peaks, (c) EIS at -0.7 V vs. RHE, (d) the on-off response, (e) FE under light illumination, and (f) comparison of FE under dark and light conditions.

interfacial factors evolved simultaneously, including changes in the local pH, modification of the interfacial dipoles, and adsorption of the CO_2-derived species, such as bicarbonates or carbonates. These processes altered the electronic structure of Ag and modified the local environment, which collectively led to the observed peak splitting, cathodic shifts and changes in the peak shape observed in Fig. 3b.

The EIS response measured at -0.7 V *vs.* RHE in the frequency region of 120 KHz–0.1 Hz with a perturbation amplitude of 10 mV shows a similar trend to the CV response shown in Fig. 3c. All the Nyquist plots for UL-Ag-STO were fitted using a two-time-constant equivalent circuit (R_s- (R_{ct1}/CPE_1)–(R_{ct2}/CPE_2)). The fitted EIS spectra (Fig. S3 and Table S1) distinguished the high-frequency process associated with electron transport across the FTO/Ag/$SrTiO_3$ interface from the Ag/STO interfacial barrier (R_{ct1}). The low-frequency process was attributed to charge transfer at the STO/PBS interface (R_{ct2}) for CO_2 reduction. The fitted values showed a decrease in both the charge-transfer resistances (R_{ct1} and R_{ct2}) when transitioning from dark to light conditions, confirming that illumination enhanced electron transport, which further accelerated the charge-transfer kinetics for the PEC CO_2 reduction. Notably, the smallest R_{ct2} in the CO_2-saturated PBS under light illumination reflected the synergistic effect of photocarrier generation and the plasmonic effect of the Ag layer on the interfacial charge-transfer kinetics. For instance, the chopped CA response also depicted an enhanced photoresponse of UL-Ag-STO

under light-illumination conditions (Fig. 3d). In contrast, the other photocathodes depicted lower current densities and higher charge-transfer resistances (R_{ct}) compared to the UL-Ag-STO sample (Fig. S3), consistent with the trend: UL-Ag-STO < M-Ag-STO < OL-Ag-STO < STO.

For product quantification, gas chromatography (GC) was employed, which indicated the formation of CO as a major PECRR product for all the photocathodes. Under a front side illumination, we observed relative changes in the faradaic efficiency as a function of the applied potentials ranging from -0.6 to -1 V *vs.* RHE. Among all the designed photocathodes, UL-Ag-STO showed a maximum FE of 60% for CO at -0.8 V *vs.* RHE under light illumination (Fig. S4 and 3e). From these observations, we demonstrated a higher selectivity and faradaic efficiency for CO at -0.8 V *vs.* RHE. To elucidate the role of photoexcitation, the faradaic efficiency towards CO selectivity was further evaluated at 0.8 V *vs.* RHE under both dark and illuminated conditions (Fig. 3f). Under relatively dark conditions, the photoinduced contributions quantitatively amounted to a threefold enhancement in the faradaic efficiency for the production of CO, thereby highlighting the positive impact has on the electrochemical reduction.

Furthermore, we highlighted that the direction of light irradiation significantly influenced photocatalytic activity, with back illumination enhancing the performance of all the cathodes. Under these conditions, UL-Ag-STO exhibited the largest
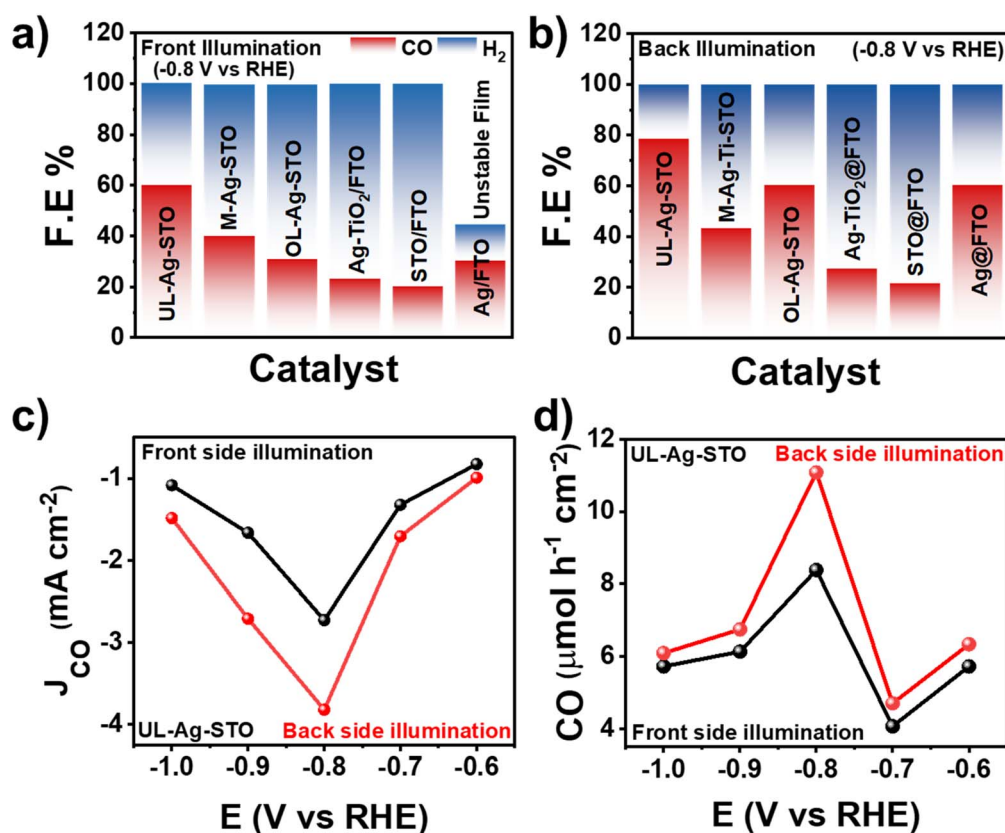

Fig. 4 FE plots for the various photocathodes at an optimum potential: (a) front side illumination, (b) backside illumination, (c) yield rate comparison, and (d) a comparison of the partial current density of CO for UL-Ag-STO under front and back illumination conditions in the CO_2-saturated PBS.

improvement, with the faradaic efficiency for CO increasing from 60% to 80%, outperforming most reported STO- and Ag-based photocathodes (Fig. 4b, Table S2 and S3 in SI). Whilst photoinduction generally benefits faradaic outputs, OL-Ag-STO and the pristine Ag photocathode films were found to be unstable in aqueous conditions under illumination, leading to a reduced photocatalytic activity compared to UL-Ag-STO (Fig. S4).

The enhanced PEC performance of the UL-Ag-STO electrode under back illumination was attributed to a combination of optical and electronic effects. Back illumination directs light through the FTO onto the plasmonic Ag layer, enabling localized surface plasmon resonance and scattering that enhances light absorption in $SrTiO_3$.[47] This configuration also favours photogenerated carrier distribution, with electron–hole pairs being generated closer to the Ag/FTO interface, promoting efficient hole collection at the back contact and minimizing electron–hole recombination. Additionally, plasmonic Ag injects hot electrons into $SrTiO_3$ under back illumination, further enhancing the kinetics of CO_2 reduction.[48] Moreover, under back illumination, the Ag layer reflects and scatters unabsorbed photons back into the $SrTiO_3$, effectively causing the light to undergo multiple internal reflections within the $SrTiO_3$.[48] This increases the effective optical path length of the photons inside it, enhancing their probability of absorption, resulting in a higher photogenerated carrier density and an improved photoelectrochemical performance.[49] Together, these factors synergistically increased the

electron flux to the catalytic surface, enabling enhanced photoelectrochemical CO_2 reduction under back illumination conditions. A 1.5-fold increase in the CO yield rate and partial current density were observed under back illumination compared to front illumination (Fig. 4c and d).

The stability of the UL-Ag-STO photocathode was demonstrated by a steady current–time (J vs. t) response curve at -0.8 V vs. RHE over 10 hours (Fig. 5a), along with subsequent cyclic repeatability tests (Fig. S5a and b). The XRD analysis of the used UL-Ag-STO photocathode (Fig. S5c) revealed no detectable phase transformation, and the SEM images showed no significant changes in surface morphology (Fig. S5d).

To elucidate the origin of the enhanced photoelectrocatalytic activity of UL-Ag-STO relative to the other crafted photocathodes, Mott–Schottky (MS) measurements were conducted at 1000 Hz over the potential range of -0.2 V to 2.0 V vs. RHE. The MS plots confirmed an n-type conductivity for all the photocathode samples (Fig. S6 (a–c)). The flatband potential, determined from the intercept of the MS plots, indicates the higher reducibility of UL-Ag-STO compared to OL-Ag-STO and the pristine STO (Fig. S6d). To further probe the photocathode/PBS interface, particularly the role of the double layer and the influence of Ag on the electronic structure of STO, the potential of zero charge (E_{PZC}) was extracted from the global minimum in the differential capacitance plots derived from the Mott–Schottky measurements performed at a frequency of 1000 Hz with a 10 mV sinusoidal perturbation
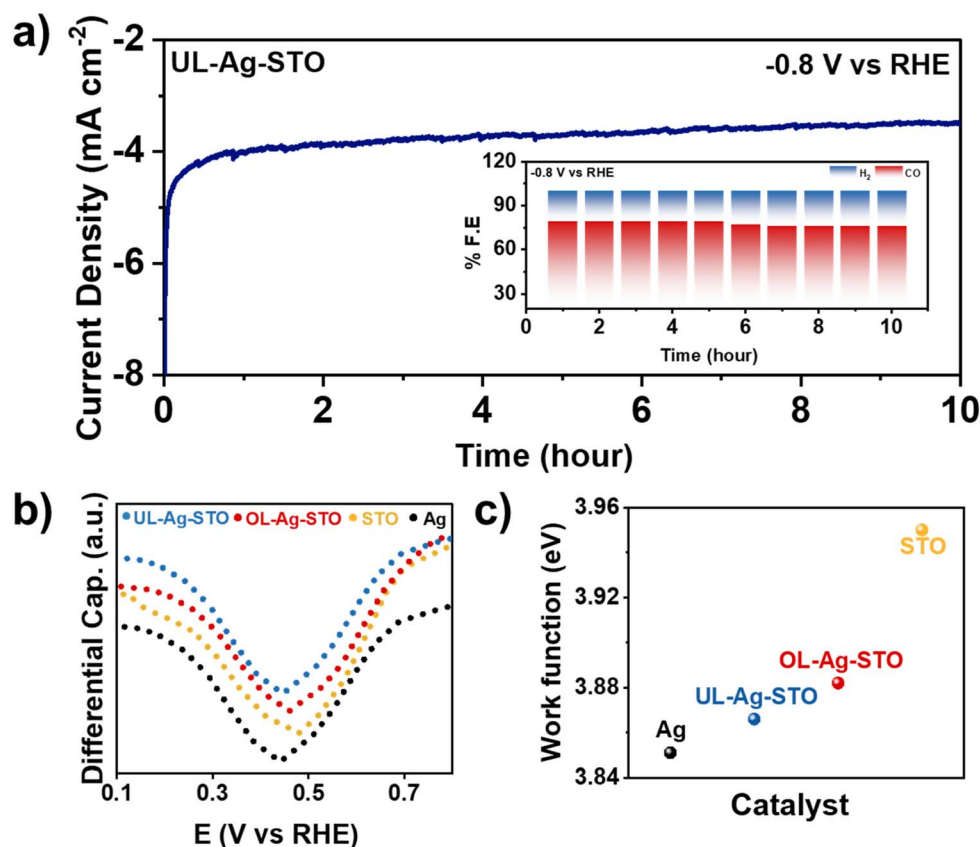

Fig. 5 (a) Long-term stability of CA at -0.8 V vs. RHE for 10 hours with an inset of the photocatalytic performance, (b) differential capacitance measurements, and (c) work function of the various photocathodes estimated from Fig. 5b.

amplitude (Fig. 5b). A rigorous protocol was employed to minimize errors in the E_{PZC} determination. Specifically, the dissolved O_2 was removed by Ar purging for 30 minutes, the electrochemical window was carefully selected, and the system was allowed to stabilise at an open-circuit potential (OCP) for 60 minutes, as previously reported. In 0.5 M PBS, UL-Ag-STO exhibited the largest E_{PZC}[32,33] shift of approximately 50 mV, indicative of a more pronounced modulation of the interfacial electric field. The larger shift in the E_{PZC} helped in regulating the interfacial electric field, stabilizing CO_2 reduction intermediates, and promoting CO production.

Moreover, the enhanced cathodic shift in UL-Ag-STO suppressed excessive proton accumulation at the interface, thereby favoring the kinetically demanding CO_2 reduction over the competing hydrogen evolution reactions. The electrochemical work function (Φ_{ad}^o) estimated from the E_{PZC} values ($\Phi_{ad}^o = E_{PZC}$ + 3.44) indicates that Ag lowered the work function of STO, with the greatest decrease for UL-Ag-STO from 4.0 eV to around 3.86 eV (Fig. 5c). This reduction in the work function enhanced conductivity and the charge-transfer kinetics, contributing to UL-Ag-STO's superior photocatalytic performance compared to the pristine STO and other photocathodes.

6.2.1 Mechanistic insights. The formation of the Ag/STO heterostructure induced interfacial-charge equilibration that fundamentally modified the electronic structure and energetics of the system.[50] Individually, FTO/STO and FTO/Ag exhibited work functions of approximately 4.99 eV and 5.3 eV, respectively. Upon heterostructure formation, the effective work function measured by Kelvin probe force microscopy (KPFM) decreased to about 4.83–4.84 eV, a reflection of the intrinsic electronic equilibration effects as a result of the metal-semiconductor coupling. Simultaneously, the operando electrochemical measurements from the potential of zero charge (E_{PZC}) yielded a significantly lower work function value (3.86 eV), corresponding to the solid–liquid interface under reaction conditions.[51,52] This discrepancy arose due to the formation of an electrical double layer (EDL), which subsequently formed interfacial dipoles due to ion adsorption, thereby screening the photogenerated electrons and mediating band bending. These effects collectively lowered the energy barrier for electron transfer at the electrode/electrolyte interface.[53,54]

More specifically, the formation of a denser cation-screening Stern layer at the electrode/electrolyte interface significantly facilitated CO_2 adsorption and the stabilisation of CO-forming intermediates by strengthening the local electric field and modulating the interfacial solvation environment.[55] Cations in the Stern layer screened the negative charges on the surface of the STO catalyst, which enhanced the local electric field near the surface and lowered the activation energy for CO_2 adsorption.[56] This electrostatic stabilisation favoured the formation and retention of intermediate species, such as CO_2^* and COOH*, which are critical for directing the reaction pathway towards CO formation, while suppressing competing reactions, such as hydrogen evolution.[57] Studies have shown that different cations impact the capacitance and electric field strength of the Stern layer, altering the kinetics and selectivity of CO_2 reduction reactions by promoting specific intermediate configurations and facilitating inner-sphere electron transfer steps.[58] In

particular, partially desolvated cations can form ionic coordination with reaction intermediates, thereby directly stabilising them and thus enhancing reaction rates and product selectivity.[59]

In terms of device architecture, under back illumination, the localised surface plasmon resonance of the silver underlayer activated pronounced plasmonic excitation, generating energetic hot electrons within the silver film. These hot electrons overcame the Schottky barrier at the Ag/STO interface and were injected into the $SrTiO_3$ conduction band. Concurrently, $SrTiO_3$ native photogenerated holes migrated towards the silver layer where they were scavenged. This directional charge flow, starting from hot electron injection from Ag to STO, combined with the hole migration from STO to Ag, resulted in a stronger built-in field, which promoted efficient charge separation, prolonged carrier lifetime, and enhanced the electron density in $SrTiO_3$. Ultimately, a higher steady-state electron density at the STO/electrolyte surface resulted in a more developed EDL (denser
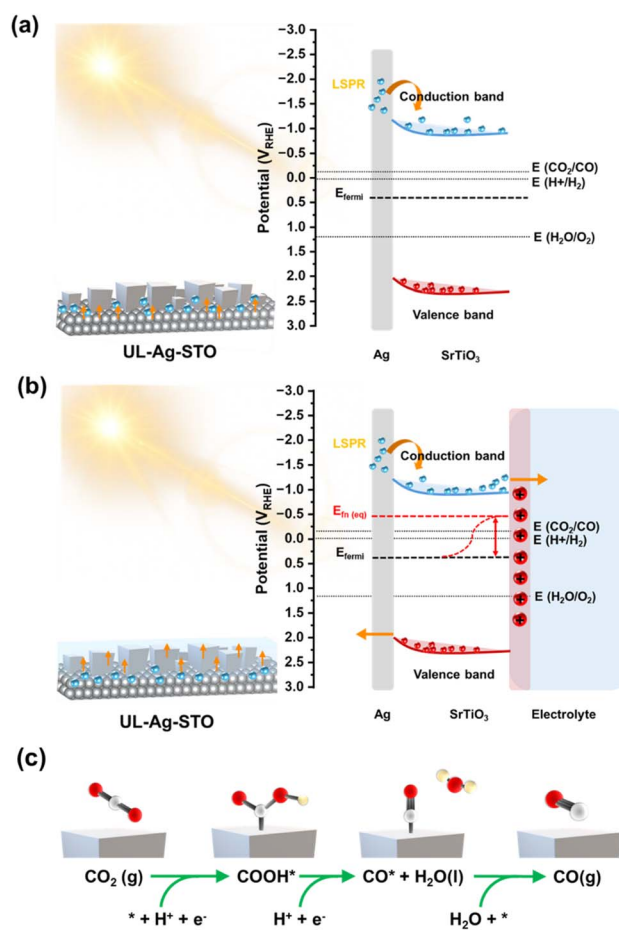

Fig. 6 (a) Initial light-mediated excitation and LSPR-mediated hot-electron transfer into $SrTiO_3$. Following these occurrences, electron accumulation and band bending increase charge separation. (b) *In situ* conditions wherein the Fermi level (E_{fermi}) of STO equilibrates with the electrolytic solution. The subsequent formation of an electrical double layer (EDL) and quasi-Fermi level splitting thermodynamically facilitates CO_2 reductive reactions *via* a new-found equilibrium. (c) Proposed reaction pathway for CO_2 reduction to CO (C atoms: grey, O atoms: red, H atoms: gold and adsorbed (*) intermediates on STO).

cationic screening), and therefore, more effective CO_2 adsorption and stabilisation of the CO-forming intermediates (Fig. 6). Comparatively, under front side illumination (electrolyte-STO-Ag), much of the light was absorbed or scattered near the STO/electrolyte surface before reaching Ag, making plasmon excitation in Ag consequently weaker, which in turn impacted the magnitude of the built-in electric field, and spatial charge separation. As a result, recombination losses increased, so fewer electrons reached the catalytic interface, and the CO_2-to-CO reaction became less efficient in comparison.

Therefore, this study, which integrates, controls, and compares the directional effects of incident illumination, achieved a high faradaic efficiency of CO (80%) and a CO production rate of 12 $\mu mol\ h^{-1}\ mg^{-1}$ at -0.8 V vs. RHE. The observed enhanced photoelectrocatalytic conversion of CO_2 to CO, and product selectivity in the Ag/STO heterostructure arose from the synergistic combination of a plasmonic hot electron injection from silver, efficient charge-carrier separation facilitated by a Schottky-barrier modulation, and effective charge screening by an electrical double layer, which fundamentally account for our observations.[33,60–62]

7 Conclusions

In summary, the integration of plasmonic Ag with STO presented a highly effective strategy for overcoming key limitations in the PEC CO_2 reduction. The underlayer architecture of UL-Ag-STO, which was developed via a simple and scalable spin-coating method, exhibited a significant enhancement in PEC performance under back illumination. This enhancement was primarily attributed to the localized surface plasmon resonance effect of Ag, which improved visible-light absorption, facilitated hot carrier injection, and prolonged charge-carrier lifetimes by reducing electron–hole recombination. As a result, the system demonstrated a high faradaic efficiency of 80% and a notable CO production rate of 12 $\mu mol\ h^{-1}\ mg^{-1}$ at -0.8 V vs. RHE. These results underline the critical role of plasmonic engineering in boosting the activity and selectivity of wide-bandgap semiconductors, such as STO, making them viable candidates for solar-to-fuel applications. Moreover, the successful demonstration of a low-cost, solution-processed thin film catalyst opens new avenues for designing efficient and scalable PEC devices for CO_2 conversion. This study contributes toward the broader goal of developing carbon-neutral technologies and highlights the promise of plasmonic-perovskite hybrid systems in addressing global energy and environmental challenges.

Author contributions

M. A.-J, G. S, A.U. B, N. R. and S. H. led the conceptualization, material characterization, electrochemical studies, data analysis, and manuscript drafting with inputs from M. A.-J. and P. P. I. The study's framework, data interpretation, and manuscript refinement were guided by M. A.-J. and P. P. I.

Conflicts of interest

There are no conflicts of interest to declare.

Data availability

The data supporting the findings of this study are available within the supplementary information (SI) and from the corresponding author upon reasonable request. Supplementary information: the supplementary data file provides extended characterisation and performance analysis supporting the main manuscript. It includes KPFM surface potential histograms, SEM imaging of surface morphologies, fitted EIS spectra under light and dark conditions with corresponding parameters, Faradaic efficiency and stability data of photocathodes, and Mott-Schottky plots with flatband potential calculations. Additionally benchmarking tables summarise the performance of similar photoelectrocatalysts, and list state-of-the-art systems for CO_2 reduction. See DOI: https://doi.org/10.1039/d5ta08539j.

Acknowledgements

Notes and references

1 K. Caldeira and J. F. Kasting, Insensitivity of global warming potentials to carbon dioxide emission scenarios, Nature, 1993, 366, 251–253.

2 S. Xu and E. A. Carter, Theoretical Insights into Heterogeneous (Photo)electrochemical CO_2 Reduction, *Chem. Rev.*, 2019, **119**, 6631–6669.

3 X. Chang, T. Wang, P. Yang, G. Zhang and J. Gong, The Development of Cocatalysts for Photoelectrochemical CO_2 Reduction, *Adv. Mater.*, 2019, **31**(31), 1804710.

4 Y. Shi and Y. Liu, Vacancy and N dopants facilitated Ti^{3+} sites activity in 3D $Ti_{3-x}C_2T_y$ MXene for electrochemical nitrogen fixation, *Appl. Catal., B*, 2021, **297**, 120482.

5 Y. Wang, *et al.*, Pulsed-Laser-Triggered Piezoelectric Photocatalytic CO_2 Reduction over Tetragonal $BaTiO_3$ Nanocubes, *Adv. Mater.*, 2023, **35**(45), 2305257.

6 B. Boga, *et al.*, Design of $SrTiO_3$-based catalysts for photocatalytic CO_2 reduction, *Catal. Sci. Technol.*, 2024, **14**, 3459–3472.

7 L. Zhang, H. H. Mohamed, R. Dillert and D. Bahnemann, Kinetics and mechanisms of charge transfer processes in photocatalytic systems: A review, *J. Photochem. Photobiol., C*, 2012, **13**, 263–276.

8 H.-J. Liu, *et al.*, Breaking the Relation between Activity and Stability of the Oxygen-Evolution Reaction by Highly Doping Ru in Wide-Band-Gap $SrTiO_3$ as Electrocatalyst, *ACS Catal.*, 2022, **12**, 6132–6142.

9 K. Shao, *et al.*, Modification of Ag nanoparticles on the surface of $SrTiO_3$ particles and resultant influence on photoreduction of CO_2, *Appl. Surf. Sci.*, 2018, **434**, 717–724.

10 S. Ezendam, *et al.*, Hybrid Plasmonic Nanomaterials for Hydrogen Generation and Carbon Dioxide Reduction, *ACS Energy Lett.*, 2022, **7**, 778–815.

11 S. A. Ali, I. Sadiq and T. Ahmad, Superlative Porous Organic Polymers for Photochemical and Electrochemical CO_2 Reduction Applications: From Synthesis to Functionality, *Langmuir*, 2024, **40**, 10414–10432.

12 S. Ezendam, *et al.*, Hybrid Plasmonic Nanomaterials for Hydrogen Generation and Carbon Dioxide Reduction, *ACS Energy Lett.*, 2022, **7**, 778–815.

13 Y. Cai, *et al.*, Theoretical exploration of CO_2 photocatalytic reduction using single atom gold nanoparticles (Au^0) modified $SrTi_{0.875}Hf_{0.125}O_3$, *J. Catal.*, 2024, **432**, 115410.

14 M. A. M. Bajiri, *et al.*, Engineering Stable Cu-Doped $SrTiO_3$ Perovskites for Enhanced Photocatalytic CO_2 Reduction, *Inorg. Chem.*, 2025, **64**, 15370–15380.

15 Q. Zhang, *et al.*, Visible-Light-Active Plasmonic Ag–$SrTiO_3$ Nanocomposites for the Degradation of NO in Air with High Selectivity, *ACS Appl. Mater. Interfaces*, 2016, **8**, 4165–4174.

16 K. Marchuk and K. A. Willets, Localized surface plasmons and hot electrons, *Chem. Phys.*, 2014, **445**, 95–104.

17 L. Zhou, Q. Huang and Y. Xia, Plasmon-Induced Hot Electrons in Nanostructured Materials: Generation, Collection, and Application to Photochemistry, *Chem. Rev.*, 2024, **124**, 8597–8619.

18 S. Shaheen and T. Ahmad, The potential of H_2 evolution and CO_2 mitigation from photochemical to electrochemical perspectives, *Chem. Commun.*, 2025, **61**, 17810–17824.

19 S. Asim Ali, M. Khanam, I. Sadiq, S. Shaheen and T. Ahmad, Physicochemical Modulations in MXenes for Carbon Dioxide Mitigation and Hydrogen Generation: Tandem Dialogue between Theoretical Anticipations and Experimental Evidences, *J. Colloid Interface Sci.*, 2025, **679**, 1046–1075.

20 S. Wan, M. Chen, M. Ou and Q. Zhong, Plasmonic Ag nanoparticles decorated $SrTiO_3$ nanocubes for enhanced photocatalytic CO_2 reduction and H_2 evolution under visible light irradiation, *J. CO_2 Util.*, 2019, **33**, 357–364.

21 J. Xue, Z. Chen, Y. Zhang and J. Zhao, A review on plasmonic enhancement of activity and selectivity in electrocatalytic CO_2 reduction, *Front. Energy*, 2024, **18**, 399–417.

22 Q. T. Trinh, *et al.*, How to design plasmonic Ag/$SrTiO_3$ nanocomposites as efficient photocatalyst: Theoretical insight and experimental validation, *J. Alloys Compd.*, 2024, **1002**, 175322.

23 I. Sadiq, S. A. Ali, S. Shaheen, I. Fatima and T. Ahmad, Unlocking potential and challenges of MOFs and COFs based energy materials for CO_2 reduction and H_2 production, *Int. J. Hydrogen Energy*, 2025, **120**, 146–180.

24 P. Kalra, M. Samolia, A. U. Bashir, V. D. Avasare and P. P. Ingole, Engineered Electron-Deficient Sites at Boron-Doped Strontium Titanate/Electrolyte Interfaces Accelerate the Electrocatalytic Reduction of N_2 to NH_3 : A Combined DFT and Experimental Electrocatalysis Study, *ACS Appl. Mater. Interfaces*, 2024, **16**, 37938–37951.

25 A. U. Bashir and P. P. Ingole, Activating the Basal Planes of Ti_2C MXene for Accelerated Ammonia Electrosynthesis: Role of Surface Terminations, *Small*, 2025, **21**, 2409457.

26 A. U. Bashir and P. P. Ingole, Understanding the Modulated Electrocatalytic H_2 Generation Activity of Surface Functionalized Ti_2C MXenes Using the Potential of Zero Charge and Electron Transfer Coefficient as Electrochemical Descriptors, *ACS Electrochem.*, 2025, **1**, 1055–1065.

27 X.-C. Ma, Y. Dai, L. Yu and B.-B. Huang, Energy transfer in plasmonic photocatalytic composites, *Light:Sci. Appl.*, 2016, **5**, e16017.

28 Z. Chen, *et al.*, Efficient Electron Transfer by Plasmonic Silver in $SrTiO_3$ for Low-Concentration Photocatalytic NO Oxidation, *Environ. Sci. Technol.*, 2022, **56**, 3604–3612.

29 D. Li, S. Yu and H. Jiang, From UV to Near-Infrared Light-Responsive Metal–Organic Framework Composites: Plasmon and Upconversion Enhanced Photocatalysis, *Adv. Mater.*, 2018, **30**, 1707377.

30 L. Wang, *et al.*, Designing p-Type Semiconductor–Metal Hybrid Structures for Improved Photocatalysis, *Angew. Chem., Int. Ed.*, 2014, **53**, 5107–5111.

31 M. Jiang, *et al.*, Hot-Electron Injection and Charge Carrier Lifetime Prolongation Enhance the Photoelectrochemical Performance of a Plasmonic CdS/Au Photoanode, *J. Phys. Chem. C*, 2021, **125**, 17109–17116.

32 P. Kalra, M. Samolia, A. U. Bashir, V. D. Avasare and P. P. Ingole, Engineered Electron-Deficient Sites at Boron-Doped Strontium Titanate/Electrolyte Interfaces Accelerate the Electrocatalytic Reduction of N_2 to NH_3 : A Combined DFT and Experimental Electrocatalysis Study, *ACS Appl. Mater. Interfaces*, 2024, **16**, 37938–37951.

33 P. Kalra, D. Ghosh and P. P. Ingole, Favoring Product Desorption by a Tailored Electronic Environment of Oxygen Vacancies in $SrTiO_3$ via Cr Doping for Enhanced and Selective Electrocatalytic CO_2 to CO Conversion, *ACS Appl. Mater. Interfaces*, 2023, **15**, 30187–30198.

34 Y. Zhang, *et al.*, Crystal Facet Engineering on $SrTiO_3$ Enhances Photocatalytic Overall Water Splitting, *J. Am. Chem. Soc.*, 2024, **146**, 6618–6627.

35 H. G. Yang, *et al.*, Anatase TiO_2 single crystals with a large percentage of reactive facets, *Nature*, 2008, **453**, 638–641.

36 T. Kimijima, K. Kanie, M. Nakaya and A. Muramatsu, Solvothermal synthesis of $SrTiO_3$ nanoparticles precisely controlled in surface crystal planes and their photocatalytic activity, *Appl. Catal., B*, 2014, **144**, 462–467.

37 F. Fang, *et al.*, Understanding targeted modulation mechanism in $SrTiO_3$ using K^+ for solar water splitting, *Appl. Catal., B*, 2022, **316**, 121613.

38 X. Ran, *et al.*, Manipulating Oxygen Vacancy in $SrTiO_3$ Nanoparticles to Achieve Enhanced Photoelectrochemical Performance in Water Splitting, *ACS Appl. Nano Mater.*, 2024, **7**, 27543–27554.

39 C. P. P. Wong, *et al.*, Enhancement of discharge capacity and energy density by oxygen vacancies in nickel doped $SrTiO_3$ as cathode for rechargeable alkaline zinc battery, *Electrochim. Acta*, 2022, **404**, 139705.

40 L. F. da Silva, *et al.*, Long-range and short-range structures of cube-like shape $SrTiO_3$ powders: microwave-assisted hydrothermal synthesis and photocatalytic activity, *Phys. Chem. Chem. Phys.*, 2013, **15**, 12386.

41 Y. Liu, J. Liang, S. Xu and Y. Geng, Surface Plasmon Field-Enhanced Raman Scattering Co-Excited by P-Polarized and S-Polarized Light Based on Waveguide-Coupled Surface Plasmon Resonance Configuration, *ACS Omega*, 2023, **8**, 41953–41959.

42 C. Awada, Plasmonic Enhanced SERS in Ag/TiO_2 Nanostructured Film: An Experimental and Theoretical Study, *Micromachines*, 2022, **13**, 1595.

43 M. R. Singh, J. D. Goodpaster, A. Z. Weber, M. Head-Gordon and A. T. Bell, Mechanistic insights into electrochemical reduction of CO2 over Ag using density functional theory and transport models, *Proc. Natl. Acad. Sci. U. S. A.*, 2017, **114**(42), 8812–8821.

44 J.-J. Li, *et al.*, Interfacial band bending induced charge-transfer regulation over $Ag@ZIF-8@g-C_3N_4$ to boost photocatalytic CO_2 reduction into syngas, *Catal. Sci. Technol.*, 2022, **12**, 3343–3355.

45 X. Liu, *et al.*, Understanding trends in electrochemical carbon dioxide reduction rates, *Nat. Commun.*, 2017, **8**, 15438.

46 D. Wrana, *et al.*, Kelvin probe force microscopy work function characterization of transition metal oxide crystals under ongoing reduction and oxidation, *Beilstein J. Nanotechnol.*, 2019, **10**, 1596–1607.

47 L. Ma, *et al.*, Enhancing photocatalysis in $SrTiO_3$ by using Ag nanoparticles: A two-step excitation model for surface plasmon-enhanced photocatalysis, *J. Chem. Phys.*, 2015, **143**, 084706.

48 Y. Tian and T. Tatsuma, Mechanisms and Applications of Plasmon-Induced Charge Separation at TiO_2 Films Loaded with Gold Nanoparticles, *J. Am. Chem. Soc.*, 2005, **127**, 7632–7637.

49 D. M. Schaadt, B. Feng and E. T. Yu, Enhanced semiconductor optical absorption via surface plasmon excitation in metal nanoparticles, *Appl. Phys. Lett.*, 2005, **86**, 063106.

50 K. Leung, First Principles Determination of the Potential-of-Zero-Charge in an Alumina-Coated Aluminum/Water Interface Model for Corrosion Applications, *J. Electrochem. Soc.*, 2022, **169**, 081502.

51 P. A. Markeev, *et al.*, Energy-Level Alignment at Interfaces between Transition-Metal Dichalcogenide Monolayers and Metal Electrodes Studied with Kelvin Probe Force Microscopy, *J. Phys. Chem. C*, 2021, **125**, 13551–13559.

52 A. Auer, X. Ding, A. S. Bandarenka and J. Kunze-Liebhäuser, The Potential of Zero Charge and the Electrochemical Interface Structure of Cu(111) in Alkaline Solutions, *J. Phys. Chem. C*, 2021, **125**, 5020–5028.

53 P. Li, Y. Jiao, J. Huang and S. Chen, Electric Double Layer Effects in Electrocatalysis: Insights from Ab Initio Simulation and Hierarchical Continuum Modeling, *JACS Au*, 2023, **3**, 2640–2659.

54 S. Czerny-Holownia, *et al.*, How the electric double layer impacts nitrate reduction to ammonia, *EES Catal.*, 2025, **3**(6), 1272–1284, DOI: 10.1039/D5EY00217F.

55 E. Johnson and S. Haussener, Contrasting Views of the Electric Double Layer in Electrochemical CO_2 Reduction: Continuum Models vs Molecular Dynamics, *J. Phys. Chem. C*, 2024, **128**, 10450–10464.

56 J. Sun and J. Wu, Unveiling Double Layer Effects in Electrocatalytic CO_2 Reduction, *J. Phys. Chem. C*, 2025, **129**, 8946–8954.

57 S. Liang, L. Huang, Y. Gao, Q. Wang and B. Liu, Electrochemical Reduction of CO_2 to CO over Transition Metal/N-Doped Carbon Catalysts: The Active Sites and Reaction Mechanism, *Adv. Sci.*, 2021, **8**, 2102886.

58 H.-G. Qin, *et al.*, Surface-immobilized cross-linked cationic polyelectrolyte enables CO_2 reduction with metal cation-free acidic electrolyte, *Nat. Commun.*, 2023, **14**, 5640.

59 V. Sinha, E. Khramenkova and E. A. Pidko, Solvent-mediated outer-sphere CO_2 electro-reduction mechanism over the Ag111 surface, *Chem. Sci.*, 2022, **13**, 3803–3808.

60 P. Sebastián-Pascual, Y. Shao-Horn and M. Escudero-Escribano, Toward understanding the role of the electric double layer structure and electrolyte effects on well-defined interfaces for electrocatalysis, *Curr. Opin. Electrochem.*, 2022, **32**, 100918.

61 T. Luo, *et al.*, Electric Double Layer Structure in Electrocatalytic Carbon Dioxide Reduction, *Adv. Energy Sustain. Res.*, 2023, **4**(3), 2200148.

62 T. Nakamoto, S. Iguchi, S. Naniwa, T. Tanaka and K. Teramura, Mg-doped $SrTiO_3$ photocatalyst with Ag–Co cocatalyst for enhanced selective conversion of CO_2 to CO using H_2O as the electron donor, *Catal. Sci. Technol.*, 2023, **13**, 4534–4541.